# Exceptional points in negatively refracting chirowaveguides due to giant chirality

Alice De Corte [1,*,†] Stefanos Fr. Koufidis [2,*,‡] Martin W. McCall [2] and Bjorn Maes [1]

[1]*Micro- and Nanophotonic Materials Group, Research Institute for Materials Science and Engineering,*
*University of Mons, 20 Place du Parc, 7000 Mons, Belgium*

[2]*Blackett Laboratory, Department of Physics, Imperial College of Science, Technology and Medicine,*
*Prince Consort Road, London SW7 2AZ, United Kingdom*

In non-Hermitian systems, particularly those adhering to $\mathcal{PT}$ symmetry, exceptional points (EPs) are critical junctures wherein eigenvalues and eigenvectors coalesce. These points induce the convergence of eigenmodes in waveguiding systems, resulting in unique dispersion features and remarkable effects such as slow light. In a configuration comprising two coupled waveguides, EPs can be achieved via mechanisms involving balanced gain-loss modulation or contradirectional modal interference. By leveraging the latter, in homogeneous chirowaveguides without any reliance on periodicity, we demonstrate the signature phase transitions induced by negative refraction due to giant chirality, which does not necessitate the simultaneous negativity of the permittivity and permeability. Our approach offers advantages over traditional $\mathcal{PT}$-symmetric and negative-refractive-index waveguides, as it does not pose the manufacturing difficulties of balancing the creation and absorption of photons while providing opportunities for remarkable light manipulation due to the presence of chirality. Experimental implementations of metamedia with giant and, moreover, controllable chirality indicate that our medium is well within reach of current technology.

## I. INTRODUCTION

Exceptional points (of degeneracy) are critical junctures in a system's parameter space wherein the eigenvalues and the corresponding eigenvectors coincide [1], indicating a deeper form of coalescence involving both [2]. This stands in direct contrast to the so-called diabolic points, where only the eigenvalues coincide [3]. Exceptional points (EPs) are particularly important in non-Hermitian systems that conform to $\mathcal{PT}$-symmetric conditions, under which real spectra can manifest [4], suggesting that the system's properties remain intact under parity reflection and time reversal. In waveguiding systems, EPs lead to the convergence of multiple eigenmodes into a single mode, resulting in distinctive dispersion relations in the vicinity of the merging point(s). Such a convergence induces a sharp reduction in group velocity (i.e., slow light) [5–7] and a substantial increase in the local density of states and photon lifetime [8], thereby enhancing the quality factor of coupled resonators [9]. Graphene-induced EPs lead to polarization-dependent photonic switching [10], while combining the nonlinear effect of saturable absorption with EPs results in reciprocity breaking in non-Hermitian coupled photonic waveguides [11].

In a photonic configuration comprising *two* coupled waveguides, Mealy and Capolino [12] identified two potential methods for achieving EPs. The first relies on non-Hermitian Hamiltonians [13], in which, within the context of $\mathcal{PT}$ symmetry, a conventional codirectional coupling exists between waveguides with modulated gain and loss [14]. By contrast, the second mechanism does not necessitate the presence of modulated gain or loss but, rather, involves the coupling between waveguides that support contradirectional modal interference. Indeed, upon fixing the wave vector corresponding to the *guided* super-mode $\mathbf{k}_s$ to point in the forward direction, the latter scenario is conceptualized in Fig. 1. In this setup, a standard waveguide, $W_A$, is coupled to another waveguide, $W_B$, in which the direction of phase propagation is opposite to the direction of the power flow, i.e., $\mathbf{k}_B \cdot \mathbf{S}_B < 0$, with $\mathbf{S}_B$ being the axial component of the transversely integrated Poynting vector (note that this is not equivalent to the group velocity; see Ref. [17]).

Implementing a $\mathcal{PT}$-symmetric grating that effectively balances photon creation (i.e., gain) and absorption (i.e., loss) poses significant challenges [18]. Consequently, current research efforts have shifted towards exploring alternative approaches, such as anti-$\mathcal{PT}$ symmetry [19], non-Bloch $\mathcal{PT}$ symmetry [20], regular or degenerate band edges [21], and virtual gain [22], to name a few. Recently, Ref. [23] demonstrated the feasibility of realizing EPs in a system of coupled waveguides, where a homogeneous dielectric slab is coupled to one with a negative refractive index. Subsequently, the same group elaborated in Ref. [24] on how anti-$\mathcal{PT}$ symmetry, induced by a negative refractive index, can lead to higher-order EPs [25], even in the absence of dissipation.

Intriguingly, an alternative avenue to achieve negative refraction exists which does not necessitate the simultaneous negativity of the permittivity and the permeability. In this paper, we diverge from conventional approaches and adopt Pendry's chiral route to negative refraction [26]. In particular, we propose a chiral system to achieve the signature phase transitions, and hence the characteristic bifurcation

---

*These authors contributed equally to this work.

†Contact author: alice.decorte@umons.ac.be

‡Contact author: steven.koufidis20@imperial.ac.uk

points in modal dispersion, without relying on the standard gain-loss modulation of Ref. [27]. Our approach leverages contradirectional coupling between a dielectric waveguide and a chirowaveguide, both of which are homogeneous and nonperiodic, without the necessity of the permittivity and permeability being simultaneously negative. Besides eliminating the need for meticulously engineering a double-negative material, chirality provides an additional degree of freedom for controlling various aspects of the apparent dispersion's "fork(s)" [28,29]. Since magnetoelectric coupling can be controlled via a plethora of methods (such as piezoelectricity [30], externally applied electric fields [31], conductivity [32], etc.), our medium offers a convenient platform for manipulating the location of the emerging EPs.

This paper is structured as follows: In Sec. II, we adapt coupled-wave theory to describe negatively refracting chirowaveguides with giant chirality and demonstrate the possibility of achieving EPs in a *single* chirowaveguide with extreme optical rotatory capabilities without resorting to any kind of loss-gain modulation. In Sec. III, our coupled-wave approach is extended to model wave propagation in a contradirectional coupler, where a conventional dielectric slab waveguide is coupled to a negatively refracting chirowaveguide. The previously identified condition for the occurrence of EPs is generalized to couplers with nonidentical waveguides, and we illustrate the predicted dispersion features and modal profiles using the SIMPHOTONICS MATLAB toolbox, a Maxwell-equations solver developed at Laboratoire Charles Fabry [29] that utilizes the finite-element method. Furthermore, we discuss how varying chirality influences the dispersion characteristics and modal profiles of the supported eigenmodes, including an interesting phenomenon of merging "broken-symmetry" complex zones, with two EPs effectively canceling each other. Finally, in Sec. IV, we summarize and propose potential approaches toward the experimental implementation of our setup.

## II. $\mathcal{PT}$-LIKE BEHAVIOR OF A CHIROWAVEGUIDE WITH GIANT CHIRALITY

### A. Coupled-wave theory description

If **E** and **B** are the primitive electromagnetic fields and **D** and **H** are the corresponding stimulated excitation fields, Tellegen's temporal-frequency-domain constitutive relations for the simplest reciprocal bi-isotropic medium read [33]

$$\mathbf{D} = \epsilon_r \epsilon_0 \mathbf{E} + i\frac{\kappa}{c}\mathbf{H} \quad \text{and} \quad \mathbf{B} = -i\frac{\kappa}{c}\mathbf{E} + \mu_r\mu_0\mathbf{H}. \quad (1)$$

Here, $\epsilon_r$ and $\mu_r$ are the relative permittivity and permeability, respectively; $\epsilon_0$ and $\mu_0$ are the corresponding parameters of free space, and $c = (\epsilon_0\mu_0)^{-1/2}$ is the phase velocity of light in vacuum. The dimensionless chirality parameter $\kappa$ measures the wavelengths after which the electric field of a linearly polarized wave is rotated by $2\pi$.

Such an *unbounded* reciprocal bi-isotropic medium supports both right- and left-handed circular polarizations [34]. Indeed, upon combining Maxwell's macroscopic source-free curl relations with the constitutive relationships of Eq. (1), the supported wave numbers turn out to be $\pm k_{(\pm)} = \pm k_0(\kappa \pm \bar{n})$, where $k_0$ is the free-space wave number and $\bar{n} = (\epsilon_r\mu_r)^{1/2}$
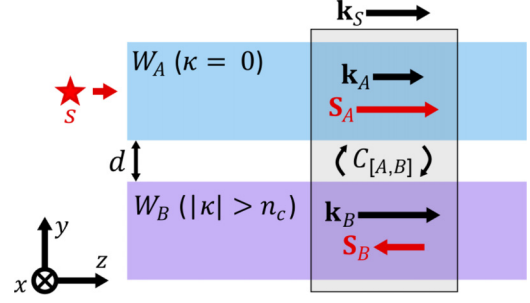


FIG. 1. Contradirectional chiral coupler: An achiral dielectric slab waveguide $W_A$ is coupled to a *homogeneous* chirowaveguide $W_B$ brought into proximity at a distance $d$. Under the indicated excitation source $s$, waveguide $W_A$ supports a forward-propagating mode, which can couple with a counterpropagating mode supported by $W_B$. For giant chirality ($|\kappa| > n_c$, where $\kappa$ represents the dimensionless chirality parameter and $n_c$ denotes the core refractive index) the chirowaveguide operates in the negative refraction regime, where the phase propagation opposes the Poynting vector (i.e., $\mathbf{k}_B \cdot \mathbf{S}_B < 0$). Whence, for stationary solutions, the wave vector of the super-mode, $\mathbf{k}_s$, points in the positive direction, albeit contra-directional coupling is attainable. Crucially, the power-flow vector pointing toward the source $\mathbf{S}_B$ is attributed to the vortexlike behavior observed in Refs. [15,16], thereby respecting causality.

is the medium's refractive index. For $|\kappa| < \bar{n}$, the *nominally* forward-propagating (F) eigenmodes are [33]

$$\mathbf{E}^{\text{F}}_{(\pm)} = E^{\text{F}}_{(\pm)} \frac{e^{ik_0(\bar{n}\pm\kappa)z}}{\sqrt{2}} \begin{pmatrix} 1 \\ \pm i \end{pmatrix}, \quad (2a)$$

whereas the backward-propagating (B) ones are

$$\mathbf{E}^{\text{B}}_{(\pm)} = E^{\text{B}}_{(\pm)} \frac{e^{-ik_0(\bar{n}\pm\kappa)z}}{\sqrt{2}} \begin{pmatrix} 1 \\ \pm i \end{pmatrix}. \quad (2b)$$

The signs within the parentheses in the phasors of the electric fields $\mathbf{E}^{\text{F,B}}_{(\pm)}$ denote the polarization state, and $E^{\text{F,B}}_{(\pm)}$ are constant amplitudes; an $e^{-i\omega t}$ dependence is herein implicit and suppressed. If $|\kappa| > \bar{n}$, the direction of phase propagation and the handedness of counterpropagating modes are interchanged [33,35], although the direction of the Poynting vector remains unaffected.

A chiral medium can sustain two orthogonal polarization states, whereas a dielectric slab waveguide can support TE and TM modes. In TE modes, one electric-field component lies out of the plane (as defined in Fig. 1), whereas in TM modes, one magnetic-field component lies out of this plane. Not surprisingly, a chirowaveguide slab sustains hybrid modes [36]. Assuming weak chirality and weak guiding, Ref. [37] approximated these modes as $f_E E_{\text{TE}} + f_M E_{\text{TM}}$, where $f_{E,M}$ are slowly varying functions of one spatial coordinate and $E_{\text{TE}}$ ($E_{\text{TM}}$) are the electric-field components of TE (TM) modes. Although such an approximation leads to simple, and thus insightful, dispersion relations, it becomes ineffective when dealing with giant chirality. Hence, we resort to the brute force of numerical calculation of the dispersion, as derived in Eqs. (22) and (23) of Ref. [38]. In fact, for a chirowaveguide surrounded by air ($n_s = 1$), with a core refractive index $n_c$, the values of $\kappa$ for which the direction of phase propagation of one mode is altered turn out to be $|\kappa| = n_c$ (note that $|\kappa| = 1$

per the nomenclature of Ref. [38]). These points correspond to those at which a reversal in the direction of phase propagation occurs in unbounded bi-isotropic media [cf. Eq. (2) for $|\kappa| \approx n_c$]. For insights into the implications of negative refraction for cutoff frequencies, consult Refs. [15,39].

For a single chirowaveguide, Lee's [40] coupled-wave theory approach identifies the unperturbed and perturbed geometries. Regarding the former, let $\mathbf{E}$ and $\mathbf{H}$ be the electric and magnetic excitation fields satisfying Maxwell's equations and the appropriate boundary conditions in a lossless reciprocal homogeneous achiral waveguide, characterized by a relative permittivity $\epsilon_r$. For the latter geometry, $\mathbf{E}'$ and $\mathbf{H}'$ will be the corresponding fields in a lossless reciprocal homogeneous chirowaveguide, characterized by a relative permittivity $\epsilon_r'$ and a chirality parameter $\kappa$. Then, the unperturbed fields associated with the $n$th proper mode are $\mathbf{E} = \mathbf{e}_n e^{ik_n z}$ and $\mathbf{H} = \mathbf{h}_n e^{ik_n z}$, where $\mathbf{e}$ and $\mathbf{h}$ are $z$-independent fields (i.e., they depend only on the transverse coordinates). As derived in Appendix A, the synthesis of Lorentz reciprocity and the orthogonality relation delineated in Appendix B yields the coupled-wave system

$$\frac{da_n}{dz} = \sum_m a_m e^{i\delta k_{mn}z} C_{mn}, \qquad (3)$$

where $a_m$ are the expansion coefficients of the transverse components of the perturbed fields (radiation modes are disregarded), $\delta k_{mn} = k_m - k_n$ are the detuning parameters, and $C_{mn}$ are the coupling coefficients.

If $S$ is the arbitrary cross section of the chirowaveguide, all overlapping terms in Eq. (3) are concisely written as

$$C_{mn} = \mathrm{sgn}(n)\frac{k_0}{2}\int_S \left(V_{mn}^{[1]} + V_{mn}^{[2]} + V_{mn}^{[3]}\right) dS. \qquad (4)$$

The first term in Eq. (4) arises due to the permittivity's perturbation, which for the current purposes is presumed to be weak (i.e., $\epsilon_r'/\epsilon_r \approx 1$), and reads

$$V_{mn}^{[1]} = i(\epsilon_r' - \epsilon_r)\mathbf{e}_n^* \cdot \mathbf{e}_m, \qquad (5a)$$

corroborating Eq. (8.20) of Ref. [40]. The second term

$$V_{mn}^{[2]} = \kappa(\mathbf{h}_n^* \cdot \mathbf{e}_m - \mathbf{e}_n^* \cdot \mathbf{h}_m), \qquad (5b)$$

is attributed to the first-order chirality terms and corroborates Eq. (24) of Ref. [41]. The third term,

$$V_{mn}^{[3]} = \kappa\frac{\kappa^2 + \bar{n}^2 - \tilde{n}^2}{\tilde{n}^2 - \kappa^2}(h_{\parallel,n}^* e_{\parallel,m} - e_{\parallel,n}^* h_{\parallel,m})$$
$$- i\frac{\kappa^2}{\tilde{n}^2 - \kappa^2}(\epsilon_r e_{\parallel,n}^* e_{\parallel,m} + \mu_r h_{\parallel,n}^* h_{\parallel,m}), \qquad (5c)$$

stems from the inclusion of higher-order chirality terms, corroborating Eq. (25) of Ref. [42]; $\tilde{n} = (\epsilon_r'\mu_r)^{1/2}$. Furthermore, for weak guiding (i.e., for $\bar{n} \approx \tilde{n}$), we note that $\lim_{\kappa \to 0}(V_{mn}^{[3]}/V_{mn}^{[2]}) = 0$, implying that in the limit of weak chirality only $V_{mn}^{[2]}$ is appreciable.

Inspection of Eqs. (5a)–(5c), verifies that $V_{mn}^{[1],[2],[3]} = -(V_{nm}^{[1],[2],[3]})^*$, $m \neq n$. Thus, for codirectional (contradirectional) coupling, in which power flows in the same (opposite) direction for both modes, we have the symmetry constraint $C_{nm} = -C_{mn}^*$ ($C_{nm} = C_{mn}^*$) [43]. Focusing on the first two terms of Eq. (3), by rotating the amplitudes per $\tilde{a}_1 = e^{-ik_1 z}a_1$

and $\tilde{a}_2 = e^{-ik_2 z}a_2$, we obtain [44]

$$\frac{d}{dz}\begin{pmatrix} \tilde{a}_1 \\ \tilde{a}_2 \end{pmatrix} = \begin{pmatrix} -ik_1 & C_{21} \\ C_{12} & -ik_2 \end{pmatrix}\begin{pmatrix} \tilde{a}_1 \\ \tilde{a}_2 \end{pmatrix}, \qquad (6)$$

where $k_{1,2}$ are the unknown propagation constants of the perturbed eigenmodes.

### B. Bifurcation point in the modal dispersion

The (weighted) superposition of the two modes interfering in the chirowaveguide constitutes the system's supermode, whose propagation constant can be found upon substituting $\tilde{a}e^{ik_s z}$, where $\tilde{a} = (\tilde{a}_1 \quad \tilde{a}_2)^{\mathsf{T}}$, with $\mathsf{T}$ denoting transpose, in Eq. (6). Algebraic manipulations yield the propagation constants of such an eigenmode, namely,

$$k_s = -\bar{k} \pm S, \qquad (7)$$

where

$$\bar{k} = \frac{k_1 + k_2}{2} \quad \text{and} \quad S = \left[\left(\frac{\delta k_{21}}{2}\right)^2 - C_{12}C_{21}\right]^{1/2}.$$

The corresponding eigenvectors turn out to be $\tilde{a} = (-2iC_{21}/(\delta k_{21} \pm S) \quad 1)^{\mathsf{T}}e^{i(\bar{k}\mp S)z}$, where it is evident that both eigenvalues and eigenvectors coalesce to $\bar{k}$ and $\tilde{a} = (-2iC_{21}/\delta k_{21} \quad 1)^{\mathsf{T}}e^{i\bar{k}z}$, respectively, when

$$S = 0 \Rightarrow \delta k_{21} = \pm 2(C_{12}C_{21})^{1/2}. \qquad (8)$$

This is the condition for the occurrence of EPs in a single chirowaveguide, in agreement with Ref. [12]. In a system devoid of gain or loss, $\delta k_{21}$ is purely real; hence, Eq. (8) implies that this requirement can be fulfilled only in instances of contradirectional coupling:

$$C_{12} = C_{21}^*. \qquad (9)$$

In the absence of any standard reflection mechanism in the chirowaveguide (e.g., a grating), a wave with a Poynting vector directed toward the source would typically require an additional excitation for *causal* power flow. This salient feature is often overlooked, precisely because eigenanalysis is inherently stationary and does not distinguish between an excitation placed at $-\infty$ or at $+\infty$ [45]. Of course, any waveguide with $z$-reversal symmetry allows for counterpropagating modes ($\mathbf{k}_z \to -\mathbf{k}_z$), with the pairs $(\mathbf{E}_\perp, -E_\parallel)$ and $(-\mathbf{H}_\perp, H_\parallel)$ also solving the wave-guiding problem. Here, $\mathbf{F} = \mathbf{F}_\perp + F_\parallel\hat{\mathbf{k}}$, with $\mathbf{F} = \{\mathbf{E}, \mathbf{H}\}$ and $\hat{\mathbf{k}}$ being a unit vector in the direction of $\mathbf{k}_s$. As noted in Ref. [15], the energy flux in the negatively refracting slab opposes that in the cladding (note that $\mathbf{k}_s$ is fixed for guided modes, as they are stationary solutions of the corresponding wave equation). This implies sustained waves may require continuous sources at both ends. However, as explicated in Ref. [15], averaging the Poynting vector over the pulse period reveals a double-vortex energy flow structure, akin to that observed in the surface modes of Ref. [16]. Such a mechanism confines energy within wave packets with minimal dissipation, thus enabling opposing directions of the Poynting vector in the core and the cladding via only one source. These considerations justify the sign function in Eq. (4), elucidate the "counterintuitive" $\mathcal{PT}$-symmetry breaking in the anisotropic waveguide of Ref. [46] that does
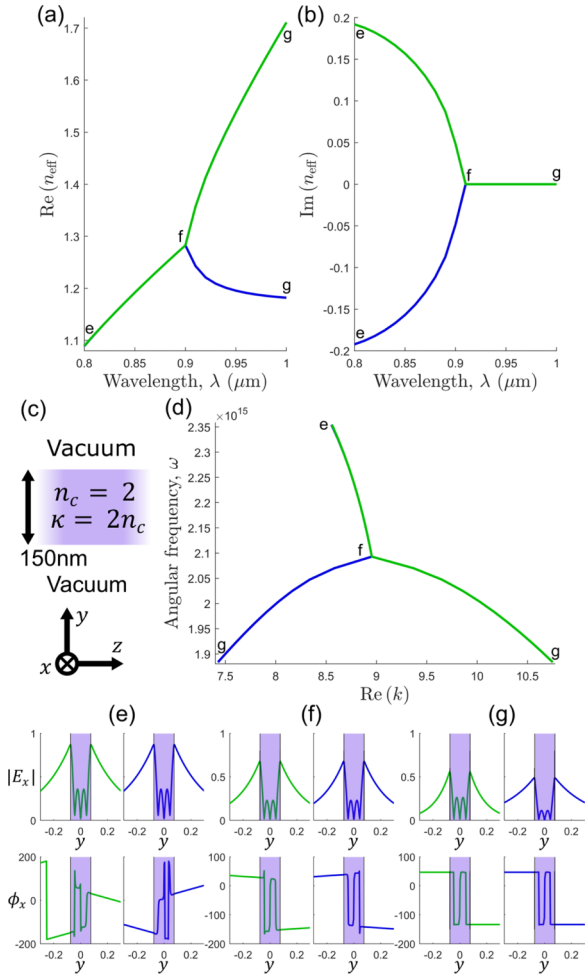
FIG. 2. Dispersion characteristics and modal profiles of a single negatively refracting chirowaveguide due to giant chirality: (a) Real and (b) imaginary parts of the refractive indices of two interfering modes supported by a 150-nm-thick chirowaveguide, with $n_c = 2$ and $\kappa = 2n_c$, embedded in vacuum. (c) Schematic of the structure with modes propagating in the $z$ direction. (d) Dispersion $\omega(k)$ of these same modes. $E_x$ component of their electric-field profiles at (e) $\lambda = 0.8$ µm, (f) $\lambda = 0.9$ µm, and (g) $\lambda = 1$ µm. The magnitude of each field is shown in the top panel, with its associated phase displayed in the bottom panel.

not possess gain or loss, and explains a negative Poynting vector (cf. Fig. 2(d) in Ref. [23]).

For a chirowaveguide slab with a thickness of 150 nm, refractive index $n_c = 2$, and chirality parameter $\kappa = 2n_c$ [see Fig. 2(c)], the guided modes are obtained using SIMPHOTONICS MATLAB. As depicted in Fig. 2(a), a $\mathcal{PT}$-like fork in the modal dispersion emerges, with a sole EP arising at the bifurcation point around $\lambda \approx 0.9$ µm. In the "$\mathcal{PT}$-broken" regime (i.e., before the EP), the effective indices of the modes exhibit equal real parts but opposite imaginary parts [see Fig. 2(b)]. Consequently, one mode propagates as a growing wave, $\tilde{a}_2 \propto e^{[C_{12}C_{21} - (\delta k_{21}/2)^2]^{1/2}z} e^{-i\bar{k}z}$, while the other attenuates, $\tilde{a}_1 \propto e^{-[C_{12}C_{21} - (\delta k_{21}/2)^2]^{1/2}z} e^{i\bar{k}z}$. In this regime, both modes are backward, as indicated by the negative group velocity [slope of $\omega(k)$ in Fig. 2(d)]. Moreover, the electric-field profiles have identical magnitudes but opposite phases [see
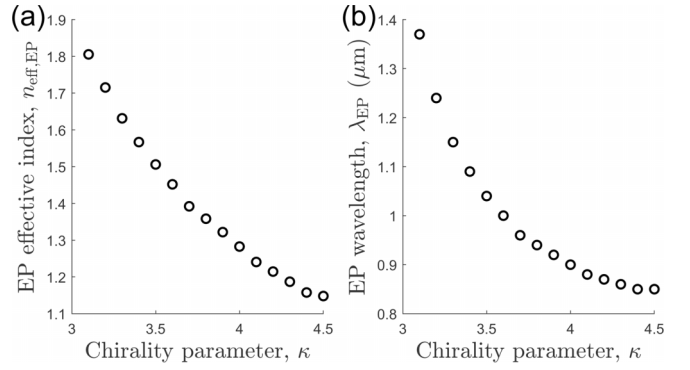


FIG. 3. Controlling EPs via the chirality parameter: (a) Real part of the refractive index and (b) wavelength of an EP arising in a 150-nm-thick chirowaveguide embedded in vacuum, with $n_c = 2$, as a function of $\kappa$. Up to a first-order approximation, the reciprocal trend becomes apparent upon scrutinizing Eqs. (8) and (5b).

Fig. 2(e)], the converse of the case of gain-loss $\mathcal{PT}$-broken modes that have asymmetric field magnitudes (see, e.g., Ref. [29]). However, in this instance, complex-index modes stem from strong coupling between counterpropagating modes [see Eq. (7)] and do not correspond to a spatial imbalance between gain and loss regions, therefore not requiring asymmetry. By contrast, precisely at the EP, the modes merge: their effective indices and profiles are identical, as shown in Fig. 2(f). Transitioning to the "$\mathcal{PT}$-symmetric" regime beyond the bifurcation point, the modes' effective refractive indices assume distinct real values. One mode is backward with a negative group velocity (green), while the other is forward with a positive group velocity (blue), as indicated by the slope of $\omega(k)$ in the bottom panel of Fig. 2(d). While the magnitudes of their electric fields differ, their phases remain equal [see Fig. 2(g)], indicating an equal number of nodes but varying field distributions.

The value of the chirality parameter strongly influences the effective refractive index of the chirowaveguide modes, thereby shifting the dispersion of the forward and backward modes and their coupling point. In the same 150-nm-thick waveguide with refractive index $n_c = 2$, we vary the chirality parameter from $1.5n_c$ to $2.25n_c$ and plot the real part of the effective refractive index of the modes at the EP as well as the wavelength at which the EP ensues. Figure 3 reveals that increasing the chirality shifts the EP to lower values of effective refractive index and shorter wavelengths, thus providing a tuning mechanism for the EP location in parameter space. A reciprocal dependence of this nature is anticipated and can be heuristically traced back to Eq. (8). Specifically, since $\bar{k} = 2\pi/\lambda_{\text{EP}} \propto \pm(C_{12}C_{21})^{1/2}$, under a first-order approximation, the quantity $(C_{12}C_{21})^{1/2}$ is proportional to $\kappa$ [see Eq. (5b)], which elucidates the illustrated reciprocal trend in Fig. 3.

## III. EXCEPTIONAL POINTS IN CONTRADIRECTIONAL CHIROWAVEGUIDE COUPLERS

### A. Coupled-wave theory description of nonidentical coupled waveguides

Hitherto, we have focused on a single chirowaveguide, with the occurrence of an EP being attributed to either an actual
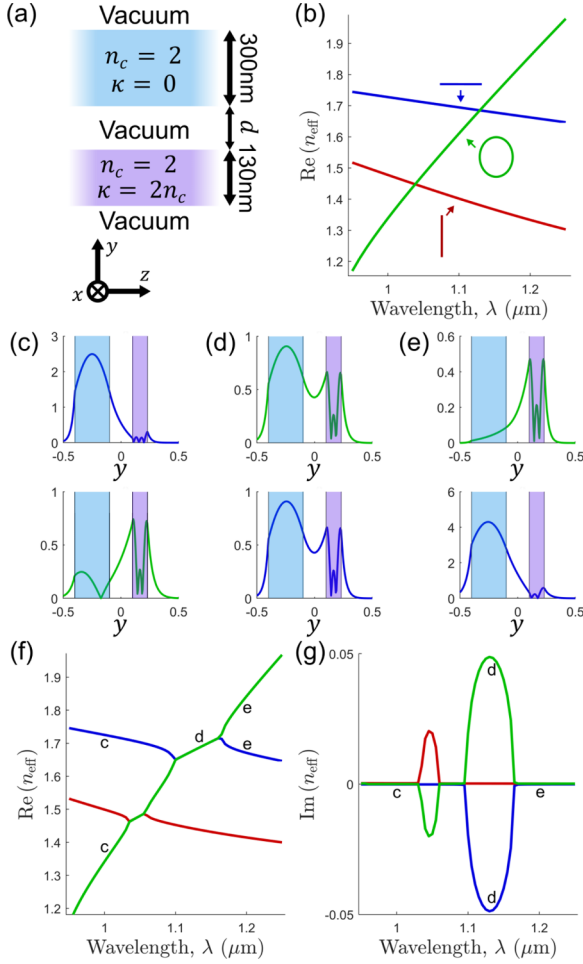
FIG. 4. Dispersion forks and modal profiles in a contradirectional chirowaveguide coupler: (a) Schematic of a 300-nm-thick dielectric slab coupled to a 130-nm-thick chirowaveguide with modes propagating in the $z$ direction. (b) Refractive indices of modes from the isolated 300-nm-thick dielectric slab waveguide (blue and red) and the 130-nm-thick chirowaveguide (green). [(c)–(e)] Profiles of the electric-field $E_x$ component for two modes of the coupled waveguides separated by 200 nm at (c) 1 μm, (d) 1.14 μm, and (e) 1.2 μm. The magnitude of the electric field's dominant $x$ component, $|E_x|$, is shown. (f) Real and (g) imaginary parts of the refractive indices of three modes interfering due to the coupling of the achiral and chiral slabs.

grating-type distributed reflection or an "effective" reflection mechanism. Proceeding to more sophisticated scenarios, one would observe that Eq. (3) can serve as the foundation for examining coupled chirowaveguides, thereby allowing one to describe the transfer of energy between the two slabs schematically depicted in Fig. 1. Specifically, a 300-nm-thick achiral slab waveguide will serve as the unperturbed geometry, whose fields will be perturbed upon bringing a 130-nm-thick chirowaveguide into proximity [see Fig. 4(a)]. Both waveguides are embedded in vacuum and have a refractive index of $n_c = 2$. The chirowaveguide has a chirality parameter of $\kappa = 2n_c$; in fact, any value of $\kappa > n_c$ would suffice.

When the two waveguides are sufficiently close, we can approximate the overall field distribution of the composite structure (i.e., the supermode) via the superposition:

$$\mathbf{E} = a_A \mathbf{e}_A e^{ik_A z} + a_B \mathbf{e}_B e^{ik_B z} \quad \text{and} \quad \mathbf{H} = a_A \mathbf{H}_A e^{ik_A z} + a_B \mathbf{H}_B e^{ik_B z},$$

where $a_A$ and $a_B$ are modal amplitudes. We may then revisit Eq. (3) and sum over $m = A, B$, therewith recasting Eq. (6) as

$$\frac{\mathrm{d}}{\mathrm{d}z} \begin{pmatrix} a_A \\ a_B \end{pmatrix} = \begin{pmatrix} -ik_A & C_{BA} \\ C_{AB} & -ik_B \end{pmatrix} \begin{pmatrix} a_A \\ a_B \end{pmatrix}, \tag{10}$$

where the detuning parameter is $\delta k_{BA} = k_B - k_A$. For the coupled configuration, the propagation constants are perturbed versions of those supported by each waveguide individually (i.e., with the other waveguide at infinity). These depend generally both on the individual waveguide mode overlap, involving integrals of the terms $\mathbf{E}_{\perp,m} \times \mathbf{h}^*_{\perp,n}$, with $\{m, n\} = \{A, B\}$, and on the perturbation to each waveguide separately [cf. Eqs. (5a)–(5c)]. The former integrals extend over all space to include radiation modes, whereas the latter are limited to the perturbation region [47]. Here, we will limit the integration area from the entire space to the perturbation region and assume that the orthogonality relation of Eq. (B4) in Appendix B is *approximately* satisfied, provided the two coupled waveguides are not *too* close. This ensures that the fields from one waveguide are minimal where those from the other are significant and vice versa [40].

Thus far, the generalization of the coupled-wave theory description from a single waveguide to coupled waveguides has been straightforward, and the condition for the occurrence of EPs, as identified in Eq. (8), seems to hold. Indeed, when coupling *identical* (or even nearly identical) waveguides to form a contradirectional coupler, the coupling coefficients are related by $C_{BA} = C_{AB}^*$. This follows from energy conservation: $\mathrm{d}/\mathrm{d}z(|a_A|^2 \pm |a_B|^2) = 0$, where the sign depends on the relative direction of power propagation [43,48].

However, for nonidentical waveguides, such as those illustrated in Fig. 1, the coupling coefficient corresponding to the coupling of a mode propagating at the achiral waveguide $W_A$ to a mode supported by the chirowaveguide $W_B$, $C_{BA}$, is given by Eq. (4). Contrarily, the disturbance of a mode in the chirowaveguide $W_B$ by a mode propagating in the achiral waveguide $W_A$ yields the coupling coefficient

$$C_{AB} = i \frac{k_0}{2} \int_{S_A} (\epsilon_r - 1)(\mathbf{e}_A \cdot \mathbf{e}_B^*) \mathrm{d}S_A, \tag{11}$$

as no other perturbation mechanism as such exists in $W_A$; $\epsilon_r$ is the relative permittivity of the medium filling $W_A$ and $W_B$, and the surrounding medium is vacuum.

Therefore, two natural questions arise: (i) is energy conservation violated, and (ii) what is the condition for realizing EPs in nonidentical couplers? Concerning the former, Ref. [47] demonstrated that by considering the individual modal overlap integrals as a first-order effect of the perturbation and disregarding any radiation mode only *after* their influence has been determined, energy conservation is *not* violated. Regarding the EP condition, it is given by

$$\delta k_{BA} = \pm 2(C_{AB} C_{BA})^{1/2}, \tag{12}$$

which requires that

$$\{C_{AB} C_{BA} \in \mathbb{R} \ | \ C_{AB} C_{BA} \geqslant 0\}. \tag{13}$$

The condition in Eq. (13) can be satisfied even if $C_{AB}$ and $C_{BA}$ are not related by complex conjugation, such as in cases

involving nonidentical coupled waveguides, provided that $\mathrm{Re}(C_{AB})\mathrm{Im}(C_{BA}) = -\mathrm{Re}(C_{BA})\mathrm{Im}(C_{AB})$. In our case, however, as shown in Table I, the coupling coefficients are real, despite the waveguides being nonidentical, thereby satisfying the condition in Eq. (13). Otherwise, no EPs can occur in a system presumed to be gain- or loss-free (see Sec. II A of Ref. [12]).

### B. Forklike dispersion features without gain-loss modulation

To demonstrate the predictions of Sec. III A, let us start by considering isolated waveguides. Their modes are studied in a wavelength range that enables simple crossings between one mode of the 130-nm-thick chirowaveguide [green in Fig. 4(b)] and the two lowest-order (i.e., highest-index) guided modes of the 300-nm-thick achiral waveguide [blue and red in Fig. 4(b)]. The achiral mode polarizations are both linear, TE for the blue mode and TM for the red mode, whereas the chirowaveguide mode has a quasicircular polarization. The achiral modes propagate forward, while the chiral mode propagates backward (i.e., the direction of phase propagation and the integrated Poynting vector are opposite), suggesting the anticipated transition to the negative refraction regime due to giant chirality.

Subsequently, the waveguides are brought into proximity by placing them at a distance $d = 200$ nm apart [see the schematic in Fig. 4(a)]. The resulting supermodes are therefore partially located in the achiral and chiral waveguides. Away from any crossings between achiral and chiral dispersions, the coupled modes tend to retain approximately the same refractive index as their isolated counterparts and are mainly located in the corresponding waveguide [short and long $\lambda$ in Figs. 4(f) and 4(g) and associated profiles in Figs. 4(c) and 4(e)]. At the crossings between the achiral and chiral dispersions, however, complex zones appear [around $\lambda = 1.05$ and 1.15 μm in Figs. 4(f) and 4(g)]. As seen in Fig. 4(d), complex-index coupled-mode profiles have identical magnitudes, as in the single chirowaveguide. Their polarizations are quasilinear in the achiral waveguide and strongly elliptical in the chiral medium, with opposite orientations and rotation directions between both modes.

These complex zones widen as the waveguides are brought closer together since the coupling between the waveguides is naturally increased. When their spacing is reduced to $d = 100$ nm, both complex zones merge, as shown in Fig. 5. Interestingly, the forward-propagating mode (blue) gradually evolves from a lower-order achiral-dominated mode ($n \approx 1.75$, $\lambda \approx 0.95$ μm) to a higher-order achiral-dominated mode ($n \approx 1.5$, $\lambda \approx 1.25$ μm) by hybridizing with the complex-index modes as it crosses their dispersion curve. Nonetheless, despite this hybridization, the center of the complex zone does not constitute a third-order EP, as evidenced by the nondegenerate imaginary indices shown in Fig. 5(b).

To demonstrate the validity of the coupled-mode theory developed in Sec. III A, we extract the mode profiles from simulations of the isolated 300-nm-thick achiral waveguide and the 130-nm-thick chirowaveguide. The coupling coefficients given by Eqs. (4) and (11) are then calculated based on integration of the isolated mode profiles, considering the adequate spacing between the waveguides and under the stated assumptions. The resulting values of the coupling coefficients
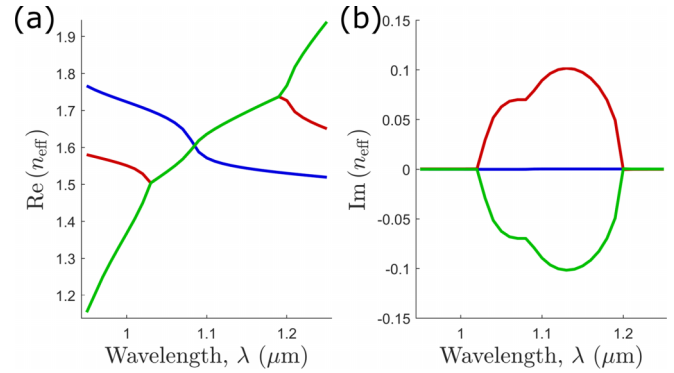


FIG. 5. Effective refractive indices supported by a contradirectional chirowaveguide coupler: (a) Real and (b) imaginary parts of the refractive indices of three modes from the 300-nm-thick achiral dielectric slab waveguide coupled to a 130-nm-thick chirowaveguide, separated by $d = 100$ nm.

are thereafter inserted into a generalized, three-mode version of the coupled-wave system [Eq. (10)], so that the effective refractive indices of the supermodes may be calculated as eigenvalues of the system:

$$\frac{\mathrm{d}}{\mathrm{d}z}\begin{pmatrix} a_1 \\ a_2 \\ a_3 \end{pmatrix} = \begin{pmatrix} -ik_1 & C_{21} & C_{31} \\ C_{12} & -ik_2 & C_{\kappa=0} \\ C_{13} & C_{\kappa=0} & -ik_3 \end{pmatrix} \begin{pmatrix} a_1 \\ a_2 \\ a_3 \end{pmatrix}, \qquad (14)$$

where subscripts 1, 2, and 3 of the coupling coefficients correspond to the chiral mode and the two achiral modes of the isolated waveguides, respectively (see Table I in Appendix C), and $k_n$ are the propagation constants of these isolated modes. The coupling between both achiral modes $C_{\kappa=0}$ is set to zero since these modes are of TE and TM nature and therefore only marginally interacting. Of course, the archetypal coupling coefficients $C_{mn}$ between two modes are described by Eq. (10), while Eq. (14) illustrates how this can be straightforwardly generalized to include three modes or, indeed, $n$ modes (see Sec. I of the supplement in Ref. [49]).

The resulting effective refractive indices are presented in Figs. 6(a) and 6(b) for a $d = 200$ nm gap and in Figs. 6(c) and 6(d) for a $d = 100$ nm gap. Clear qualitative agreement with the simulation results is noted from these plots: two complex zones for the $d = 200$ nm gap and one large, *merged*, complex zone for the $d = 100$ nm gap. Although these zones emerge at precisely the wavelengths predicted by the simulations, the theory appears to slightly overestimate their associated linewidths. This disparity stems from the interaction of a multitude of other modes in the simulation not considered in the idealized three-mode system used in theory. These other simulated modes alter the final dispersion much less significantly than the coupling occurring at dispersion crossings. We note that $V^{[3]}$ of Eq. (5c) contributes to about half the value of coupling coefficients $C_{21}$ and $C_{31}$ (see Table I in Appendix C), demonstrating the importance of considering this term for large values of chirality. Our theoretical framework is capable of analyzing chirowaveguides with non-negligible (in this instance, giant) chirality, with its success being evident upon comparing the simulation results of Figs. 4 and 5 with the theoretical predictions of Fig. 6.
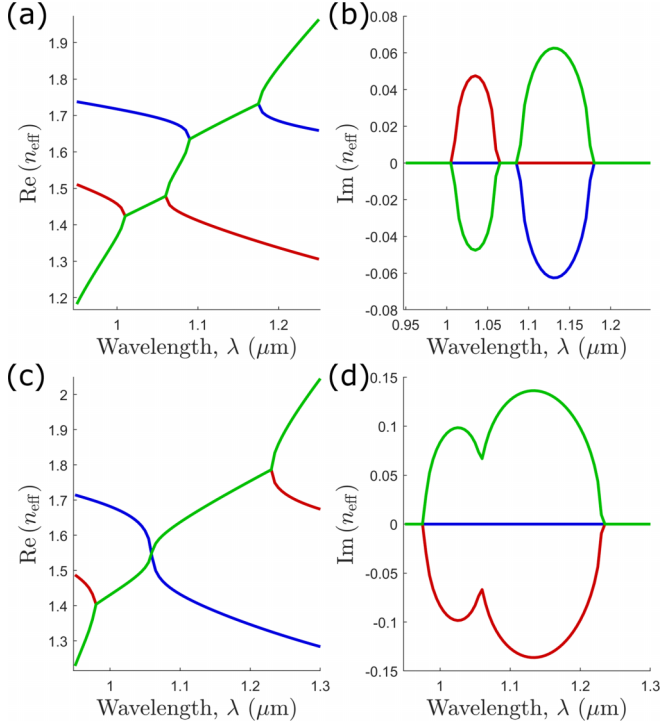
FIG. 6. Coupled-wave theory predictions for the spectral features of a chirowaveguide contradirectional coupler: Effective refractive indices of three modes theoretically calculated from Eq. (10) by integrating isolated waveguide modes extracted from simulations (a) and (b) for a $d = 200$ nm wide gap and (c) and (d) for a $d = 100$ nm wide gap. Here, (a) and (c) depict the real part of the effective refractive index, while (b) and (d) illustrate its imaginary part. For the values of the coupling coefficients obtained from the simulation, refer to Appendix C.

## IV. FURTHER DISCUSSION AND CONCLUDING REMARKS

Over three decades ago, when interest in chirowaveguides was burgeoning, approximations based on weak chirality were well founded. This was due to the inherently weak optical rotatory power of natural media, necessitating advanced structures to detect chiral responses. For instance, blue light passing through 1 mm of a $Bi_{12}GeO_{20}$ crystal has its electric field rotated by $42°$, corresponding to a chirality parameter $\kappa \approx 5.6 \times 10^{-5}$ [50]. However, recent advancements in metamaterials have unlocked the potential for giant chirality values across the electromagnetic spectrum, including optical [51,52], terahertz [53,54], and gigahertz [55,56] frequencies. For example, the metasurface reported in [51], which comprises pairs of vertically displaced dielectric bars, exhibited a chirality reaching up to $\kappa \in (2.98, 3.02)$ in the visible range of 596–604 nm. For insights into various aspects of giant chirality (maximum value, bandwidths, controllability), the reader is referred to Sec. 6 of Ref. [35] and the references therein.

Building on these developments, we proposed a chiral system to achieve signature phase transitions and characteristic bifurcations in modal dispersion without the need for gain-loss modulation as described in Ref. [27]. Our approach employs contradirectional coupling between a dielectric

waveguide and a chirowaveguide, with the latter exhibiting negative refraction due to giant chirality. Importantly, this method operates in homogeneous, nonperiodic media, circumventing the requirement for simultaneous negativity of the permittivity and permeability. This presents several advantages over traditional $\mathcal{PT}$-symmetric and negative-refractive-index waveguides. Notably, it presents a flexible alternative to current manufacturing processes while offering an additional degree of freedom for manipulating the characteristic forks in the dispersion of media such as those in Refs. [28,29].

Furthermore, the magnetoelectric coupling in our medium can be dynamically adjusted through various means such as voltage [57], pneumatic force [58], piezoelectricity [30], externally applied electric fields [31], and conductivity [32]. In addition to the usual degrees of freedom for tuning EPs, such as the refractive index, geometrical dimensions of the waveguides, etc., our approach uniquely leverages the flexibility of chirality to provide more versatile and precise control over the location of EPs. This versatility positions our system as a promising platform for advanced light manipulation, enabling precise control over optical properties. It paves the way for innovative applications in high-sensitivity integrated photonic sensors [59], gain enhancement in lasing applications [60], and topological waveguiding [61], among others.

## APPENDIX A: COUPLED-WAVE-EQUATIONS DERIVATION

Maxwell's macroscopic source-free curl relations for the unperturbed achiral waveguide are

$$\nabla \times \mathbf{E} = ik_0\mu_r\mathbf{h} \quad \text{and} \quad \nabla \times \mathbf{h} = -ik_0\epsilon_r\mathbf{E}, \quad (A1)$$

where $\mathbf{h} = \eta_0\mathbf{H}$, with $\eta_0 = (\mu_0/\epsilon_0)^{1/2}$. Accordingly, for the perturbed chirowaveguide, we have

$$\nabla \times \mathbf{E}' = k_0\kappa\mathbf{E}' + ik_0\mu_r\mathbf{h}', \quad (A2a)$$

$$\nabla \times \mathbf{h}' = -ik_0\epsilon_r'\mathbf{E}' + k_0\kappa\mathbf{h}', \quad (A2b)$$

where $\mathbf{h}' = \eta_0\mathbf{H}'$. Lorentz reciprocity dictates that [41]

$$\nabla \cdot (\mathbf{E}^* \times \mathbf{h}' + \mathbf{E}' \times \mathbf{h}^*)$$
$$= ik_0(\epsilon_r' - \epsilon_r)\mathbf{E}^* \cdot \mathbf{E}' + \kappa k_0(\mathbf{h}^* \cdot \mathbf{E}' - \mathbf{E}^* \cdot \mathbf{h}'), \quad (A3)$$

with the asterisk (∗) denoting complex conjugation. Integrating over a volume $V$, enclosed by a surface $S$, Gauss's theorem yields

$$\int_S (\mathbf{E}^* \times \mathbf{h}' + \mathbf{E}' \times \mathbf{h}^*) \mathrm{d}S$$
$$= ik_0 \int_V (\epsilon_r' - \epsilon_r)\mathbf{E}^* \cdot \mathbf{E}' \mathrm{d}V + k_0 \int_V \kappa(\mathbf{h}^* \cdot \mathbf{E}' - \mathbf{E}^* \cdot \mathbf{h}') \mathrm{d}V. \quad (A4)$$

Let the longitudinal dimension of the waveguide slab align with the $z$ axis, let $S$ denote the surface of a rectangular parallelepiped enclosing the slab at infinity, and let $\Delta z$ be the longitudinal (infinitesimal) length. The transverse surface $S_t$ is positioned such that its center of mass lies on the $z$ axis, indicated by a unit vector $\hat{\mathbf{z}}$. Furthermore, assuming an $e^{i\mathbf{k}\cdot\mathbf{r}}$ dependence for each field, we may decompose the fields as $\mathbf{F} = \mathbf{F}_\perp + F_\parallel\hat{\mathbf{k}}$, where $\mathbf{F} = \{\mathbf{E}, \mathbf{h}, \mathbf{E}', \mathbf{h}'\}$ and $\hat{\mathbf{k}}$ is a unit vector in the direction of the wave vector $\mathbf{k}$, which coincides with $\hat{\mathbf{z}}$ for axial propagation. As $\Delta z$ tends to zero, Eq. (A4) yields

$$\int_S \frac{\partial}{\partial z}(\mathbf{E}_\perp^* \times \mathbf{h}_\perp' + \mathbf{E}_\perp' \times \mathbf{h}_\perp^*) \cdot \hat{\mathbf{z}}\mathrm{d}S$$
$$= ik_0 \int_S (\epsilon_r' - \epsilon_r)\mathbf{E}^* \cdot \mathbf{E}'\mathrm{d}S + k_0 \int_S \kappa(\mathbf{h}^* \cdot \mathbf{E}' - \mathbf{E}^* \cdot \mathbf{h}')\mathrm{d}S. \tag{A5}$$

For the $n$th discrete proper mode supported by the unperturbed waveguide, we have

$$\mathbf{E} = \mathbf{e}_n e^{ik_n z}, \qquad \mathbf{h} = \mathbf{h}_n e^{ik_n z}, \tag{A6}$$

where $k_n$ is the wave number associated with the mode; per the aforesaid decomposition, $\mathbf{e}_n = \mathbf{e}_{\perp,n} + e_{\parallel,n}\hat{\mathbf{z}}$, and $\mathbf{h}_n = \mathbf{h}_{\perp,n} + h_{\parallel,n}\hat{\mathbf{z}}$. The transverse components of the unperturbed fields, as detailed in Appendix B, are well established as forming a complete set of orthonormal basis. Therefore, by disregarding any coupling or scattering by continuous radiating modes, we can expand the perturbed fields using such a basis and express them as

$$\mathbf{E}_\perp' = \sum_m a_m \mathbf{e}_{\perp,m} e^{ik_m z}, \tag{A7a}$$

$$\mathbf{h}_\perp' = \sum_m a_m \mathbf{h}_{\perp,m} e^{ik_m z}, \tag{A7b}$$

where $a_m$ are $z$-dependent amplitudes.

Defining $\nabla_\perp = \nabla - (\partial/\partial z)\hat{\mathbf{z}}$, and provided that $\kappa \neq \tilde{n}$, $\tilde{n} = (\epsilon_r'\mu_r)^{1/2}$, Eqs. (A2a) and (A2b) lead to

$$E_\parallel'\hat{\mathbf{z}} = \frac{k_0^{-1}\kappa}{\kappa^2 - \tilde{n}^2}\nabla_\perp \times \mathbf{E}_\perp' - \frac{ik_0^{-1}\mu_r}{\kappa^2 - \tilde{n}^2}\nabla_\perp \times \mathbf{h}_\perp',$$

$$h_\parallel'\hat{\mathbf{z}} = \frac{ik_0^{-1}\epsilon_r'}{\kappa^2 - \tilde{n}^2}\nabla_\perp \times \mathbf{E}_\perp' + \frac{k_0^{-1}\kappa}{\kappa^2 - \tilde{n}^2}\nabla_\perp \times \mathbf{h}_\perp'.$$

Thus, upon substitution of the expanded perturbed fields of Eqs. (A7a) and (A7b) we obtain, respectively,

$$E_\parallel' = \sum_m a_m\left(\frac{\bar{n}^2}{\tilde{n}^2 - \kappa^2}e_{\parallel,m} - \frac{i\kappa\mu_r}{\tilde{n}^2 - \kappa^2}h_{\parallel,m}\right)e^{ik_m z}, \tag{A8a}$$

$$h_\parallel' = \sum_m a_m\left(\frac{\bar{n}^2}{\tilde{n}^2 - \kappa^2}h_{\parallel,m} + \frac{i\kappa\epsilon_r}{\tilde{n}^2 - \kappa^2}e_{\parallel,m}\right)e^{ik_m z}. \tag{A8b}$$

If we set $\kappa = 0$, our expressions reproduce the result of Sec. 8.5 of Ref. [40]; for $\epsilon_r' \equiv \epsilon_r$, Eqs. (A8a) and (A8b) corroborate Eqs. (16) and (17) of Ref. [41], respectively.

As highlighted by Kamenetskii [42], expressing the longitudinal perturbed fields exclusively in terms of the corresponding component of the unperturbed fields does not inherently follow from the assumption that $\kappa \ll \tilde{n}$ and overlooks the effects of longitudinal polarization currents, which become significant near cutoff frequencies. Hence, here, we

retain the expansions of Eqs. (A8a) and (A8b) and represent the total perturbed fields

$$\mathbf{E}' = \sum_m a_m\mathbf{e}_m e^{ik_m z} + E_\kappa'\hat{\mathbf{z}}, \tag{A9a}$$

$$\mathbf{h}' = \sum_m a_m\mathbf{h}_m e^{ik_m z} + h_\kappa'\hat{\mathbf{z}}. \tag{A9b}$$

The first terms on the right-hand sides of Eqs. (A9a) and (A9b) are akin to those of Eqs. (18) and (19) in Ref. [41], respectively, showcasing the expansion of the perturbed fields in relation to the unperturbed fields. By contrast to Ref. [62], in this paper, we have additionally included

$$E_\kappa' = \sum_m a_m\left(\frac{\kappa^2 + \bar{n}^2 - \tilde{n}^2}{\tilde{n}^2 - \kappa^2}e_{\parallel,m} - \frac{i\kappa\mu_r}{\tilde{n}^2 - \kappa^2}h_{\parallel,m}\right)e^{ik_m z},$$

$$h_\kappa' = \sum_m a_m\left(\frac{\kappa^2 + \bar{n}^2 - \tilde{n}^2}{\tilde{n}^2 - \kappa^2}h_{\parallel,m} + \frac{i\kappa\epsilon_r}{\tilde{n}^2 - \kappa^2}e_{\parallel,m}\right)e^{ik_m z},$$

with $\lim_{\kappa\to 0} E_\kappa' = 0$ and $\lim_{\kappa\to 0} h_\kappa' = 0$. We emphasize that neither $E_\kappa'$ nor $h_\kappa'$ exclusively represents the *total* longitudinal component of each field.

If the unperturbed fields are those of Eq. (A6) and the perturbed fields are those of Eqs. (A9a) and (A9b), by exploiting Eq. (B6), Eq. (A5) yields

$$\mathrm{sgn}(n)\delta_{m,n}\sum_m\left[\frac{\partial a_m}{\partial z} + i\delta k_{mn}a_m\right]e^{i\delta k_{mn}z} = \sum_m a_m e^{i\delta k_{mn}z}I_{mn}. \tag{A10}$$

Finally, we may cast Eq. (A10) in the more familiar form of Eq. (6), where all integrand terms may be concisely expressed as per Eq. (4) in the main text.

## APPENDIX B: ORTHONORMAL BASIS IN DIELECTRIC WAVEGUIDES

If we remove both perturbations from Eq. (A5), i.e., set $\epsilon_r' \equiv \epsilon_r$ and $\kappa = 0$, we obtain

$$\int_S \frac{\partial}{\partial z}(\mathbf{E}_\perp^* \times \mathbf{h}_\perp' + \mathbf{E}_\perp' \times \mathbf{h}_\perp^*) \cdot \hat{\mathbf{z}}\mathrm{d}S = 0. \tag{B1}$$

In this case, the primed fields are supported by the unperturbed geometry too. Thus, we may drop the prime notation and state that the achiral waveguide supports an $n$ mode, $(\mathbf{E}_n, \mathbf{h}_n)^\mathsf{T}e^{ik_n z}$, and an $m$ mode, $(\mathbf{E}_m, \mathbf{h}_m)^\mathsf{T}e^{ik_m z}$. Thus, Eq. (B1) is rewritten as

$$(k_m - k_n)\int_S(\mathbf{E}_{\perp,n}^* \times \mathbf{h}_{\perp,m} + \mathbf{E}_{\perp,m} \times \mathbf{h}_{\perp,n}^*) \cdot \hat{\mathbf{z}}\mathrm{d}S = 0, \tag{B2}$$

where for $k_m \neq k_n$ the integral is obviously zero.

Here, we adopt the convention of Ref. [40]: $-m$ denotes a mode whose phase propagates in the opposite direction relative to that of the $m$ mode but has the same phase velocity as the latter. With the indices being arbitrary, we replace $m$ with $-m$ in Eq. (B2) and obtain

$$(k_m + k_n)\int_S(-\mathbf{E}_{\perp,n}^* \times \mathbf{h}_{\perp,m} + \mathbf{E}_{\perp,m} \times \mathbf{h}_{\perp,n}^*) \cdot \hat{\mathbf{z}}\mathrm{d}S = 0. \tag{B3}$$

We note that in deriving Eq. (B3), we have considered that our structure respects the $z$-reversal symmetry. This implies

that by replacing $k$ with $-k$, it is $\mathbf{E}_{\perp,m}$ and $-\mathbf{h}_{\perp,m}$ that satisfy Maxwell's equations. Again, for $k_m \neq -k_n$, the integral in Eq. (B3) is zero.

Adding the two conditionally zero integrals yields

$$\int_S (\mathbf{E}_{\perp,m} \times \mathbf{h}_{\perp,n}^*) \cdot \hat{\mathbf{z}} \mathrm{d}S = 0, \qquad \text{(B4)}$$

which holds true provided that $n \neq \pm m$. If $n = \pm m$, it is straightforward to show (see Ref. [40]) that the integral of Eq. (B4) is, indeed, the Poynting power density, i.e.,

$$\frac{1}{2}\mathrm{Re}\left[\int_S (\mathbf{E}_{\perp,n} \times \mathbf{h}_{\perp,n}^*) \cdot \hat{\mathbf{z}} \mathrm{d}S\right] = \mathrm{sgn}(n)P_n, \qquad \text{(B5)}$$

where $P_n$ is the power carried by the $n$th mode. The sign function ensures that upon reversing the direction of propagation the power density remains positive.

All the above are compactly summarized by

$$\int_S (\mathbf{E}_{\perp,m} \times \mathbf{h}_{\perp,n}^*) \cdot \hat{\mathbf{z}} \mathrm{d}S = \mathrm{sgn}(n)2P_n\delta_{m,n}, \qquad \text{(B6)}$$

where $\delta_{m,n}$ is the Kronecker delta. Equation (B6) shows that the power carried by any electromagnetic field in the unperturbed waveguide is the sum of the powers of all supported modes. Thus, we can expand any electric or magnetic field in the waveguide using these modes.

### APPENDIX C: COUPLING COEFFICIENTS

Table I provides the coupling coefficient values used in Eq. (14) in Sec. III B to generate Fig. 6.

TABLE I. Coupling coefficients between one mode of a 130-nm-thick slab waveguide with giant chirality (subscript 1) and two modes of a 300-nm-thick achiral slab waveguide (subscripts 2 and 3).

|          | $d = 100$ nm | $d = 200$ nm |
|----------|--------------|--------------|
| $C_{12}$ | 0.114        | 0.054        |
| $C_{21}$ | 0.087        | 0.041        |
| $C_{13}$ | 0.037        | 0.020        |
| $C_{31}$ | 0.086        | 0.046        |

[1] W. D. Heiss, The physics of exceptional points, J. Phys. A **45**, 444016 (2012).

[2] H. Kazemi, M. Y. Nada, T. Mealy, A. F. Abdelshafy, and F. Capolino, Exceptional points of degeneracy induced by linear time-periodic variation, Phys. Rev. Appl. **11**, 014007 (2019).

[3] J. Wiersig, Distance between exceptional points and diabolic points and its implication for the response strength of non-Hermitian systems, Phys. Rev. Res. **4**, 033179 (2022).

[4] C. E. Rüter, K. G. Makris, R. El-Ganainy, D. N. Christodoulides, M. Segev, and D. Kip, Observation of parity-time symmetry in optics, Nat. Phys. **6**, 192 (2010).

[5] A. Figotin and I. Vitebskiy, Slow wave phenomena in photonic crystals, Laser Photonics Rev. **5**, 201 (2011).

[6] N. Gutman, C. Martijn de Sterke, A. A. Sukhorukov, and L. C. Botten, Slow and frozen light in optical waveguides with multiple gratings: Degenerate band edges and stationary inflection points, Phys. Rev. A **85**, 033804 (2012).

[7] T. Goldzak, A. A. Mailybaev, and N. Moiseyev, Light stops at exceptional points, Phys. Rev. Lett. **120**, 013901 (2018).

[8] M. A. K. Othman, F. Yazdi, A. Figotin, and F. Capolino, Giant gain enhancement in photonic crystals with a degenerate band edge, Phys. Rev. B **93**, 024301 (2016).

[9] M. Y. Nada, M. A. K. Othman, O. Boyraz, and F. Capolino, Giant resonance and anomalous quality factor scaling in degenerate band edge coupled resonator optical waveguides, J. Lightwave Technol. **36**, 3030 (2018).

[10] D. Chatzidimitriou and E. E. Kriezis, Optical switching through graphene-induced exceptional points, J. Opt. Soc. Am. B **35**, 1525 (2018).

[11] D. Chatzidimitriou, A. Pitilakis, T. Yioultsis, and E. E. Kriezis, Breaking reciprocity in a non-Hermitian photonic coupler with saturable absorption, Phys. Rev. A **103**, 053503 (2021).

[12] T. Mealy and F. Capolino, Exceptional points of degeneracy with indirect band gap induced by mixing forward and backward propagating waves, Phys. Rev. A **107**, 012214 (2023).

[13] C. M. Bender and S. Boettcher, Real spectra in non-Hermitian Hamiltonians having $\mathcal{PT}$ symmetry, Phys. Rev. Lett. **80**, 5243 (1998).

[14] Z. Lin, H. Ramezani, T. Eichelkraut, T. Kottos, H. Cao, and D. N. Christodoulides, Unidirectional invisibility induced by $\mathcal{PT}$-symmetric periodic structures, Phys. Rev. Lett. **106**, 213901 (2011).

[15] I. V. Shadrivov, A. A. Sukhorukov, and Y. S. Kivshar, Guided modes in negative-refractive-index waveguides, Phys. Rev. E **67**, 057602 (2003).

[16] K.-Y. Kim, J. Kim, I.-M. Lee, and B. Lee, Analysis of transverse power flow via surface modes in metamaterial waveguides, Phys. Rev. A **85**, 023840 (2012).

[17] P. Kinsler and M. W. McCall, Causality-based criteria for a negative refractive index must be used with care, Phys. Rev. Lett. **101**, 167401 (2008).

[18] T. Kottos, Broken symmetry makes light work, Nat. Phys. **6**, 166 (2010).

[19] Y. Choi, C. Hahn, J. W. Yoon, and S. H. Song, Observation of an anti-$\mathcal{PT}$-symmetric exceptional point and energy-difference conserving dynamics in electrical circuit resonators, Nat. Commun. **9**, 2182 (2018).

[20] Y.-M. Hu, H.-Y. Wang, Z. Wang, and F. Song, Geometric origin of non-Bloch $\mathcal{PT}$ symmetry breaking, Phys. Rev. Lett. **132**, 050402 (2024).

[21] T. Mealy and F. Capolino, General conditions to realize exceptional points of degeneracy in two uniform coupled transmission lines, IEEE Trans. Microwave Theory Tech. **68**, 3342 (2020).

[22] H. Li, A. Mekawy, A. Krasnok, and A. Alù, Virtual parity-time symmetry, Phys. Rev. Lett. **124**, 193901 (2020).

[23] L.-T. Wu, X.-Z. Zhang, R.-Z. Luo, and J. Chen, Non-Hermitian guided modes and exceptional points using loss-free negative-index materials, Opt. Express **31**, 14109 (2023).

[24] X.-Z. Zhang, L.-T. Wu, R.-Z. Luo, and J. Chen, Higher-order exceptional points using lossfree negative-index materials, Phys. Scr. **98**, 095511 (2023).

[25] I. Mandal and E. J. Bergholtz, Symmetry and higher-order exceptional points, Phys. Rev. Lett. **127**, 186601 (2021).

[26] J. B. Pendry, A chiral route to negative refraction, Science **306**, 1353 (2004).

[27] S. Droulias, I. Katsantonis, M. Kafesaki, C. M. Soukoulis, and E. N. Economou, Chiral metamaterials with symmetry and beyond, Phys. Rev. Lett. **122**, 213201 (2019).

[28] A. De Corte and B. Maes, Tailoring of electric dipoles for highly directional propagation in parity-time-symmetric waveguides, Phys. Rev. A **106**, 023509 (2022).

[29] A. De Corte, M. Besbes, H. Benisty, and B. Maes, Chiral materials to control exceptional points in parity-time-symmetric waveguides, Phys. Rev. A **109**, 023531 (2024).

[30] W. J. Choi, G. Cheng, Z. Huang, S. Zhang, T. B. Norris, and N. A. Kotov, Terahertz circular dichroism spectroscopy of biomaterials enabled by kirigami polarization modulators, Nat. Mater. **18**, 820 (2019).

[31] Q. Zhang, E. Plum, J.-Y. Ou, H. Pi, J. Li, K. F. MacDonald, and N. I. Zheludev, Electrogyration in metamaterials: Chirality and polarization rotatory power that depend on applied electric field, Adv. Opt. Mater. **9**, 2001826 (2021).

[32] M. Liu, E. Plum, H. Li, S. Li, Q. Xu, X. Zhang, C. Zhang, C. Zou, B. Jin, J. Han, and W. Zhang, Temperature-controlled optical activity and negative refractive index, Adv. Funct. Mater. **31**, 2010249 (2021).

[33] M. W. McCall and S. F. Koufidis, Reverse circular Bragg phenomenon, Phys. Rev. Res. **4**, 043154 (2022).

[34] I. Lindell, A. Sihvola, S. Tretyakov, and A. J. Viitanen, *Electromagnetic Waves in Chiral and Bi-isotropic Media* (Artech House, London, 1994).

[35] S. F. Koufidis and M. W. McCall, Wavelength-independent Bragg-like reflection in uniaxial bi-anisotropic media, J. Opt. Soc. Am. B **40**, 2829 (2023).

[36] N. Engheta and P. Pelet, Modes in chirowaveguides, Opt. Lett. **14**, 593 (1989).

[37] M. Chien, Y. Kim, and H. Grebel, Mode conversion in optically active and isotropic waveguides, Opt. Lett. **14**, 826 (1989).

[38] G. E. Antoniou, P. K. Koivisto, and I. V. Lindell, Dispersion curves and fields for a chiral slab waveguide, IEE Proc. D: Control Theory Appl. **138**, 327 (1991).

[39] A. Alù and N. Engheta, Guided modes in a waveguide filled with a pair of single-negative (SNG), double-negative (DNG), and/or double-positive (DPS) layers, IEEE Trans. Microwave Theory Tech. **52**, 199 (2004).

[40] D. L. Lee, *Electromagnetic Principles of Integrated Optics* (Wiley, New York, 1986), Chap. 8.

[41] P. Pelet and N. Engheta, Coupled-mode theory for chirowaveguides, J. Appl. Phys. **67**, 2742 (1990).

[42] E. O. Kamenetskii, Mode interactions in chirowaveguides, J. Appl. Phys. **79**, 8899 (1996).

[43] A. Yariv, On the coupling coefficients in the "coupled-mode" theory, Proc. IRE **46**, 1956 (1958).

[44] S. F. Koufidis and M. W. McCall, Möbius transformation and coupled-wave theory: Complete identification of the transfer matrix, Phys. Rev. A **106**, 062213 (2022).

[45] E. Feigenbaum, N. Kaminski, and M. Orenstein, Negative dispersion: A backward wave or fast light? Nanoplasmonic examples, Opt. Express **17**, 18934 (2009).

[46] W. Chen, Z. Xiong, J. Xu, and Y. Chen, Generalized coupled-mode formalism in reciprocal waveguides with gain, loss, anisotropy, or bianisotropy, Phys. Rev. B **99**, 195307 (2019).

[47] A. Hardy and W. Streifer, Coupled mode theory of parallel waveguides, J. Lightwave Technol. **3**, 1135 (1985).

[48] A. Yariv, Coupled-mode theory for guided-wave optics, IEEE J. Quantum Electron. **9**, 919 (1973).

[49] H. Qi, Y. Li, X. Wang, Y. Li, X. Li, X. Wang, X. Hu, and Q. Gong, Dynamically encircling exceptional points in different Riemann sheets for orbital angular momentum topological charge conversion, Phys. Rev. Lett. **132**, 243802 (2024).

[50] P. V. Lenzo, E. G. Spencer, and A. A. Ballman, Optical activity and electrooptic effect in bismuth germanium oxide ($Bi_{12}GeO_{20}$), Appl. Opt. **5**, 1688 (1966).

[51] M. V. Gorkunov, A. A. Antonov, and Y. S. Kivshar, Metasurfaces with maximum chirality empowered by bound states in the continuum, Phys. Rev. Lett. **125**, 093903 (2020).

[52] J. Wu, H. Jiang, Z. Guo, Y. Sun, Y. Li, and H. Chen, Giant optical chirality in dielectric metasurfaces induced by toroidal dipole resonances, Opt. Lett. **48**, 916 (2023).

[53] S. Zhang, Y.-S. Park, J. Li, X. Lu, W. Zhang, and X. Zhang, Negative refractive index in chiral metamaterials, Phys. Rev. Lett. **102**, 023901 (2009).

[54] J. Zhou, D. R. Chowdhury, R. Zhao, A. K. Azad, H.-T. Chen, C. M. Soukoulis, A. J. Taylor, and J. F. O'Hara, Terahertz chiral metamaterials with giant and dynamically tunable optical activity, Phys. Rev. B **86**, 035448 (2012).

[55] E. Plum, J. Zhou, J. Dong, V. A. Fedotov, T. Koschny, C. M. Soukoulis, and N. I. Zheludev, Metamaterial with negative index due to chirality, Phys. Rev. B **79**, 035407 (2009).

[56] J. Zhou, J. Dong, B. Wang, T. Koschny, M. Kafesaki, and C. M. Soukoulis, Negative refractive index due to chirality, Phys. Rev. B **79**, 121104(R) (2009).

[57] T. Kan, A. Isozaki, N. Kanda, N. Nemoto, K. Konishi, M. Kuwata-Gonokami, K. Matsumoto, and I. Shimoyama, Spiral metamaterial for active tuning of optical activity, Appl. Phys. Lett. **102**, 221906 (2013).

[58] T. Kan, A. Isozaki, N. Kanda, N. Nemoto, K. Konishi, H. Takahashi, M. Kuwata-Gonokami, K. Matsumoto, and I. Shimoyama, Enantiomeric switching of chiral metamaterial for terahertz polarization modulation employing vertically deformable MEMS spirals, Nat. Commun. **6**, 8422 (2015).

[59] J. Wiersig, Enhancing the sensitivity of frequency and energy splitting detection by using exceptional points: Application to microcavity sensors for single-particle detection, Phys. Rev. Lett. **112**, 203901 (2014).

[60] M. Veysi, M. A. K. Othman, A. Figotin, and F. Capolino, Degenerate band edge laser, Phys. Rev. B **97**, 195107 (2018).

[61] S. A. Hassani Gangaraj and F. Monticone, Topological waveguiding near an exceptional point: Defect-immune, slow-light, and loss-immune propagation, Phys. Rev. Lett. **121**, 093901 (2018).

[62] N. Engheta and P. Pelet, Mode orthogonality in chirowaveguides, IEEE Trans. Microwave Theory Tech. **38**, 1631 (1990).